Crossover from Germanite to Renierite-Type Structures in Cu 22– x Zn x Fe 8 Ge 4 S 32 Thermoelectric Sulfides

Ventrapati Pavan Kumar, Laura Paradis-Fortin, Pierric Lemoine, Gérard Le Caër, Bernard Malaman, Philippe Boullay, Bernard Raveau, Gabin Guelou, Emmanuel Guilmeau

Crossover from germanite to renierite-type structures in $Cu_{22-x}Zn_xFe_8Ge_4S_{32}$ thermoelectric sulfides

Ventrapati Pavan Kumar,[1] Laura Paradis-Fortin,[1,2] Pierric Lemoine,[2,*] Gérard Le Caër,[3] Bernard Malaman,[4] Philippe Boullay,[1] Bernard Raveau,[1] Gabin Guélou,[1] and Emmanuel Guilmeau[1,*]

[1] CRISMAT, CNRS, Normandie Univ, ENSICAEN, UNICAEN, 14000 Caen, France

[2] Univ Rennes, CNRS, ISCR – UMR 6226, F-35000 Rennes, France

[3] Univ Rennes, CNRS, IPR – UMR 6251, F-35000 Rennes, France

[4] Institut Jean Lamour, UMR 7198 CNRS – Université de Lorraine, 2 allée André Guinier-Campus ARTEM, BP 50840, 54011 Nancy Cedex, France

Keywords: germanite, renierite, disorder, sulfide, thermoelectric

Abstract

Copper-rich sulfides with the composition $Cu_{22-x}Zn_xFe_8Ge_4S_{32}$ ($0 \leq x \leq 2$) have been investigated. The detailed structural study combining powder X-ray diffraction, electron microscopy and Mössbauer spectroscopy shows a crossover from a germanite-type domain for $0 \leq x \leq 0.4$ to a renierite-type domain for $1.2 \leq x \leq 2.0$, with a biphasic region for $x = 0.8$. Both sulfides are *p*-type thermoelectrics due to the presence of the conductive "Cu-S" network containing univalent copper as a major cationic element. All these sulfides exhibit a semiconducting behavior. However, the renierite-type sulfides show a higher resistivity and a lower thermal conductivity than the germanite ones. As a consequence, the *ZT* figures of merit are similar for germanite and renierite domains reaching values of around 0.23 at 700 K.

Introduction

Natural minerals involving copper-rich sulfides represent a huge source for designing new *p*-type thermoelectric materials. This originates from the fact that, in these systems, the major metallic element is univalent copper which is able to form, with sulfur, various tetrahedral conductive "Cu-S" frameworks. The association of CuS_4 tetrahedra with MS_4 tetrahedra of numerous metallic elements (namely M = Cr, V, Fe, Ge, Nb, Mo, Sn, Sb, Ta, W) allows not only the geometry of the conductive "Cu-S" network to be diversified but also offers the possibility of tuning the hole carrier density ("Cu^{2+} concentration") by varying the charge balance. In this way, several classes of *p*-type thermoelectric sulfides, derivatives of natural minerals, have been synthesized. Bornite Cu_5FeS_4,[1–4] tetrahedrite $Cu_{12-x}T_xSb_{14}S_{13}$ (with T = Mn, Ni, Zn, Fe),[5–12] kesterite Cu_2ZnSnS_4,[13,14] stannoidite $Cu_8Fe_3Sn_2S_{12}$,[15] germanite $Cu_{22}Fe_8Ge_4S_{32}$,[16] and colusite $Cu_{26}T_2M_6S_{32}$ (with T = V, Cr, Nb, Mo, Ta, W and M = Ge, Sn),[17–23] are among the best performing thermoelectric sulfides to date.

Among all those copper-based minerals, the natural renierite $(Cu,Zn)_{22}Fe_8(Ge,As)_4S_{32}$ [24] has not been considered to date as a potential thermoelectric candidate in spite of its formula close to that of synthetic germanite $Cu_{22}Fe_8Ge_4S_{32}$ and its structure closely related to germanite and colusite.[16,22] Based on the analysis of the close structural relationships between germanite and renierite, we have investigated the $Cu_{22-x}Zn_xFe_8Ge_4S_{32}$ series. Herein, we show a crossover from the germanite to the renierite-type structure as the zinc content increases from x = 0 to x = 2 with a biphasic state for x = 0.8. We observe that the transport properties are significantly influenced by an increase of the Zn content and that the ZT values are comparable for germanite and renierite-type structure compounds with different compositions, *i.e.* x = 0 and x = 1.2, respectively. This behavior stems from the fact that the renierite-type sulfides exhibit a higher resistivity and a lower thermal conductivity than the germanite ones.

Experimental Section

Polycrystalline samples of $Cu_{22-x}Zn_xFe_8Ge_4S_{32}$ ($0 \leq x \leq 2$) were synthesized by mechanical alloying followed by spark plasma sintering. All sample preparations and handling of powders were performed in an argon filled glovebox with oxygen content <1 ppm. Stoichiometric amounts of Cu (99.9%, Alfa Aesar), Fe (99.9%, Alfa Aesar), Zn (99.9%, Alfa Aesar), Ge (99.999%, Alfa Aesar), and S (99.99%, Alfa Aesar) were loaded in a 25 mL tungsten carbide jar under argon atmosphere. High-energy ball milling was performed in a Fritsch Pulverisette 7 Premium line planetary ball mill operating at room temperature (RT) at a disc rotation speed of 600 rpm. The jar contains 7 balls of 10 mm diameter. Jar and balls are made of tungsten carbide with a powder-to-ball weight ratio of 1:14. Powders were milled in an argon atmosphere for 6 h. The resulting powders were ground and sieved down to 150 μm. Powders were then placed in graphite dies of 10 mm diameter and densified by spark plasma sintering (SPS-FCT HPD 25) at 873 K for 30 min under a pressure of 64 MPa (heating and cooling rate of 50 and 20 K/min, respectively). This produced 10 mm diameter pellets, *ca*. 7 mm thick, with geometrical densities greater than 96% of the crystallographic value.

Powder X-ray diffraction (PXRD) measurements were performed using a D8 advance diffractometer with silicium band LynxEye detector (Cu Kα radiation with Ge (111) monochromator). Data were collected with the addition of 6 scans over the angular range $10 \leq 2\theta/^\circ \leq 140^\circ$ with a step size of 0.0105°, and a step time of 1.3 s. PXRD patterns were refined by Le Bail analysis using the *FullProf* and *WinPlotr* software packages.[25,26] The shape of the diffraction peaks was modeled using a pseudo-Voigt profile function. Zero-point shift, lattice and asymmetry parameters were systematically refined, and the background contribution was manually estimated. Room temperature Hall effect measurements were carried out using the Physical Properties Measurement System (PPMS; Quantum Design) under an applied magnetic field up to 9 T. However, it is difficult to extract reliable carrier concentrations due to an

anomalous contribution. Attempts to calculate the carrier concentration using the approximation of single parabolic band conduction model, using the formula $p = 1/R_H e$, where e is the electronic charge, gives unrealistic values. ^{57}Fe Mössbauer spectra were measured at T = 300 K in transmission geometry with a spectrometer operated in the conventional constant acceleration mode. Polycrystalline absorbers, with natural abundance of ^{57}Fe and thickness of ~15 mg cm^{-2}, were used. Sources were kept at room temperature (RT) to collect ^{57}Fe Mössbauer spectra. The source was ^{57}Co in Rh matrix with a nominal strength of 25 mCi. Velocity calibration was performed against a 12-μm-thick α-Fe foil at RT. ^{57}Fe isomer shifts (δ) are referred to α-Fe at RT. The area fraction, that is associated to a given Mössbauer site, is the fraction of the total area comprised between the spectrum and its background measured far from resonance peaks. If the Lamb-Mössbauer factors are all equal at RT, an assumption done here, the area fraction of a site gives also the fraction of Fe atoms it represents. Mössbauer spectra were fitted with a least-squares method program assuming Lorentzian peaks.

Precession electron diffraction tomography (PEDT)[27,28] data were obtained using a JEOL 2010 (200 kV) transmission electron microscope (TEM) equipped with a side-mounted Gatan Orius CCD camera and a Nanomegas Digistar unit. Samples for TEM investigations were prepared by smoothly crushing powder under ethanol in an agate mortar and depositing drops of the mixture onto a holey carbon membrane supported by a Ni grid. 100 and 86 PED patterns were collected, respectively, on $x = 0$ and $x = 2$ $Cu_{22-x}Zn_xFe_8Ge_4S_{32}$ crystals with a precession angle of 1.2° and a tilt step about 1° between each pattern. PEDT data were processed using the programs PETS 2.0[29] and Jana2006.[30]

The electrical resistivity (ρ) and Seebeck coefficient (S) were measured simultaneously from ingots, from 300 K up to 700 K using an ULVAC-ZEM3 instrument under partial helium pressure. A NETZSCH LFA-457 apparatus was used for measuring the thermal diffusivity under argon flow. The thermal conductivity (κ) was determined as the product of the

geometrical density, the thermal diffusivity, and the theoretical heat capacity using the Dulong−Petit approximation. The lattice contribution to the thermal conductivity (κ_L) was determined by subtracting the estimated electronic component (κ_e) from the measured total thermal conductivity, κ. The electronic contribution, κ_e, was derived from the Wiedemann-Franz law, $\kappa_e = L\sigma T$, where the Lorenz number, L, was approximated from the Seebeck coefficient using the single parabolic band (SPB) model.[31–33] This model was derived from the Boltzmann transport equation under the relaxation time approximation and we assumed a carrier relaxation time limited by acoustic phonon scattering, *i.e.* a scattering factor r = -1/2.

The estimated measurement uncertainties are 6% for the Seebeck coefficient, 8% for the electrical resistivity, 11% for the thermal conductivity, and 16% for the final figure of merit, ZT.[34]

Analysis of the germanite and renierite structures.

In order to understand the relationship between the structure and the thermoelectric properties of these sulfides, a careful analysis of their structures is absolutely necessary, all the more so because they exhibit complex cationic ordering phenomena which have not been fully described in the literature. Both structures derive from the ZnS sphalerite structure (cubic space group $F\overline{4}3m$) but differ from each other by their crystal symmetry: germanite is cubic $P\overline{4}3n$ ($a \sim 10.5$ Å) whereas renierite is tetragonal $P\overline{4}2c$ ($a \sim c \sim 10.5$ Å), a feature which allows them to be easily differentiated from powder X-ray diffraction study (See below).

The natural germanite, which cubic structure was determined by Tettenhorst and Corbato from powder X-ray analysis,[35] is characterized by the copper rich formula $Cu_{26}Fe_4Ge_4S_{32}$. It contains a large amount of Cu^{2+}, a feature rarely observed in synthetic copper sulfides, which probably originates from the high pressure conditions generally associated with natural mineral

formation. This structure derives from that of the well-known ZnS sphalerite (**Fig. 1a**). It consists of a semi-ordered sphalerite framework [$Cu_{24}Fe_4Ge_4S_{32}$] built up of CuS_4, FeS_4 and GeS_4 corner-shared tetrahedra (**Fig. 1b**). According to Tettenhorst, in this framework, the 6*c*, 6*d* and 12*f* sites are occupied by Cu, whereas Fe and Ge are statistically distributed over the same 8*e* site. The sphalerite network forms interstitial tetrahedral sites, among which, according to the authors, the 2*a* site is filled with remaining Cu atoms (**Fig. 1b**). The latter CuS_4 tetrahedra share their edges with the CuS_4 tetrahedra of the 12*f* sites. Note that these cations would form centered octahedral clusters $Cu_{2a}(Cu_{12f})_6$ similar to the CuL_6 clusters with L = V, Ta, Cr, Mo, W previously described for colusites.[22,36]

The synthetic germanite with a cubic structure (space group $P\bar{4}3n$) was recently obtained but with a different chemical formula $Cu_{22}Fe_8Ge_4S_{32}$,[16] supporting the above statement that divalent copper rich sulfides are rarely stabilized. In this study, the two Cu cations of this formula were in a first approach formally attributed to the 2*a* site in compliance with Tettenhorst's study.[35] However, a coupled single crystal X-ray and Mössbauer investigation of this sulfide, currently in progress, shows that the 2*a* site is fully occupied by Fe^{3+} cations. Thus, the synthetic germanite structure (**Fig. 1c**) exhibits a semi-ordered sphalerite framework, also built up of CuS_4, FeS_4 and GeS_4 tetrahedra but with a different composition [$Cu_{22}Fe_6Ge_4S_{32}$]. The distribution of the Cu, Fe and Ge cations over the 12*f,* 6*c,* 6*d* and 8*e* sites shows signature of preferential occupancy of several of them by the remaining iron but is currently not definitely established and will not be discussed further. In contrast to the natural germanite, it appears clearly that the interstitial tetrahedral 2*a* site occupied by iron forms FeS_4 tetrahedra sharing their edges with the LS_4 tetrahedra arising from L cations of the 12*f* site. Importantly, the values of the Fe_{2a}-L_{12f} distances close to 2.73 Å observed for this compound show that it exhibits octahedral metallic clusters FeL_6 similar to those encountered in colusites.[22,36]

The natural renierite $(Cu,Zn)_{22}Fe_8(Ge,As)_4S_{32}$ exhibits a structure (**Fig. 1d**) and a formula closely related to that of the synthetic germanite.[24] This sulfide also derives from the sphalerite structure but exhibits a tetragonal distortion of the latter ($a \sim c \sim 10.5$ Å). Thus, it can be described as a semi-ordered but tetragonally distorted sphalerite framework $[Cu_{22-x}Zn_xFe_8(Ge,As)_4S_{32}]$ built up of corner-shared CuS_4, FeS_4, ZnS_4 and GeS_4 tetrahedra. The cationic distribution in the different sites of this network appears to be more ordered compared to synthetic germanite: 4*g,* 4*i,* 4*m* and 8*n* sites are occupied by copper, and 4*h* and 2*f* sites are occupied by iron, whereas zinc and the remaining copper are randomly distributed over the 2*e* site, and germanium and arsenic are located on a 4*j* site.[24] Remarkably, this sphalerite framework also hosts Fe^{3+} as an interstitial cation in the 2*b* site (referring to $P\bar{4}2c$ space group). As with synthetic germanite, the corresponding FeS_4 tetrahedron shares its edges with the surrounding polyhedra, *i.e.* with 4 CuS_4 tetrahedra arising from copper on the 4*g* and 4*m* sites and 2 FeS_4 tetrahedra arising from iron on the 4*h* site. Thus, alike germanite, renierite exhibits octahedral metallic FeL_6 clusters, but differently, metal *L* apices are occupied in an ordered way, with two apical iron cations and four equatorial copper cations. This results in an elongation of those $Fe[Cu_4Fe_2]$ octahedra with 4 equatorial Fe-Cu distances of 2.65-2.67 Å and 2 longer apical Fe-Fe distances of 2.81 Å,[24] in agreement with the Fe^{3+}-Cu^{2+} and Fe^{3+}-Fe^{3+} Coulomb repulsions. Note that the average distance between central Fe^{3+} and the surrounding *L* cations in octahedral metallic FeL_6 clusters is equivalent in both structures, synthetic germanite and renierite.

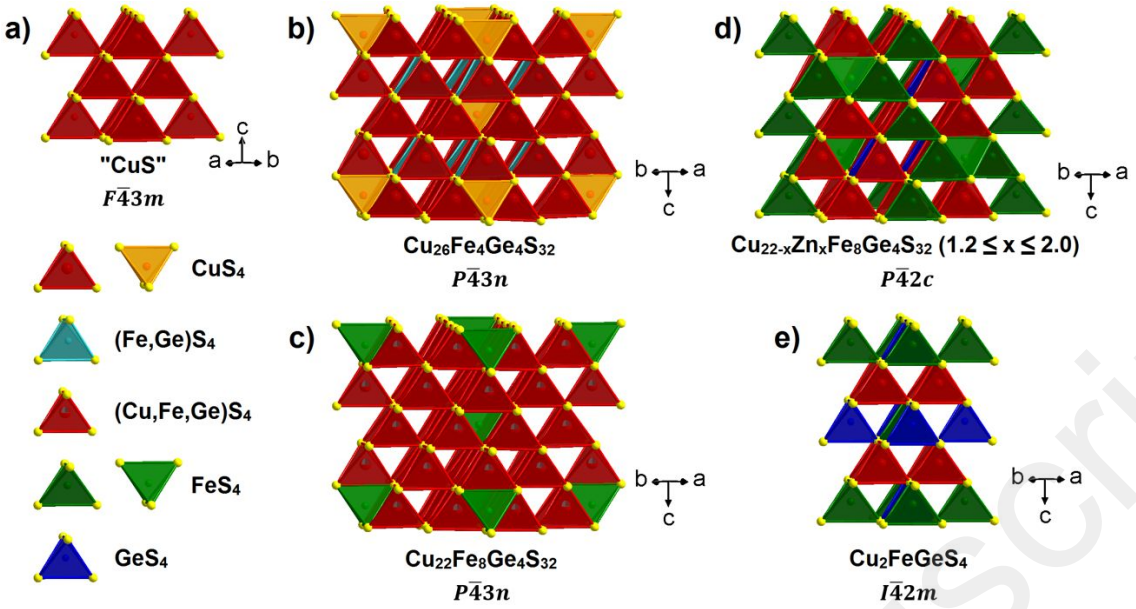

Figure 1. Crystal structure representations highlighting the semi-ordered cation distribution of (a) sphalerite "CuS", (b) mineral germanite $Cu_{26}Fe_4Ge_4S_{32}$, (c) synthetic germanite $Cu_{22}Fe_8Ge_4S_{32}$, (d) renierite $Cu_{22-x}Zn_xFe_8Ge_4S_{32}$ ($1.2 \leq x \leq 2.0$) and (e) briartite Cu_2FeGeS_4.

Results and Discussion

Structure analysis

In the following, we will show that under the same experimental conditions as those previously used for the preparation of the synthetic germanite $Cu_{22}Fe_8Ge_4S_{32}$,[16] two series of compounds can be synthesized in the system $Cu_{22-x}Zn_xFe_8Ge_4S_{32}$: a single phase germanite domain for $0 \leq x \leq 0.4$ and a single phase renierite one for $1.2 \leq x \leq 2.0$, with a biphasic domain for $x = 0.8$ corresponding to a mixture of the two sulfides.

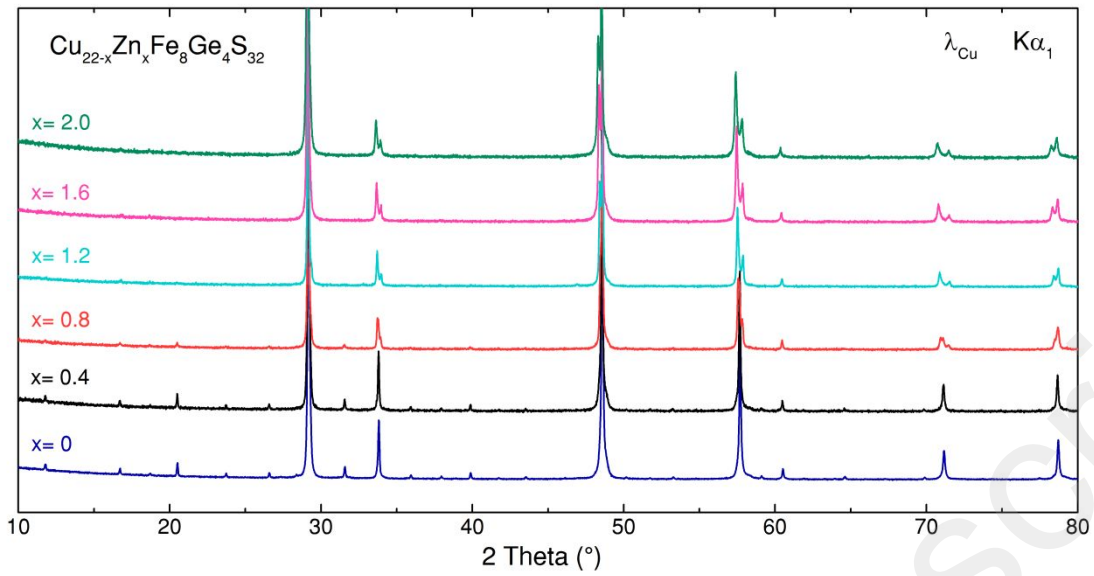

Figure 2. PXRD patterns in the $Cu_{22-x}Zn_xFe_8Ge_4S_{32}$ ($0 \leq x \leq 2$) series.

The PXRD patterns (**Fig. 2**) of the germanite samples (*i.e.* $x = 0$ and $x = 0.4$) show similarities with those of the renierite samples (*i.e.* $x = 1.2$, 1.6 and 2.0), due to the fact that the two structures have similar cell dimensions. However, the distortion of the structure from cubic in germanite to tetragonal in renierite induces a splitting of equivalent reflections either into two reflections (for (*hhl*) and (*hkk*) reflections allowed by the cubic space group) or into three reflections (for (*hkl*) reflections allowed by the cubic space group). This is illustrated by the splitting of the (622) peak of the cubic germanite into the non-equivalent intensity (622) and (226) peaks of the tetragonal renierite (**Fig. 3a**). In contrast, the (*hhh*) reflections are the only ones which are not splitted by the cubic to tetragonal distortion, as shown from the main intensity (222) diffraction peak (**Fig. 3b**) which is similar in renierite and germanite (**Fig. 2**). Note also that the reflection conditions imposed by the two different space groups also allow the germanite and renierite to be clearly distinguished from their PXRD patterns, showing that (*hhl*), (*hkk*), and (*hkh*) reflections with $l = 2n + 1$, $h = 2n + 1$, and $k = 2n + 1$, respectively, are systematically absent in the $P\bar{4}3n$ space group of germanite, whereas the tetragonal space group $P\bar{4}2c$ of renierite requires that only (*hhl*) reflections with $l = 2n + 1$ are absent.

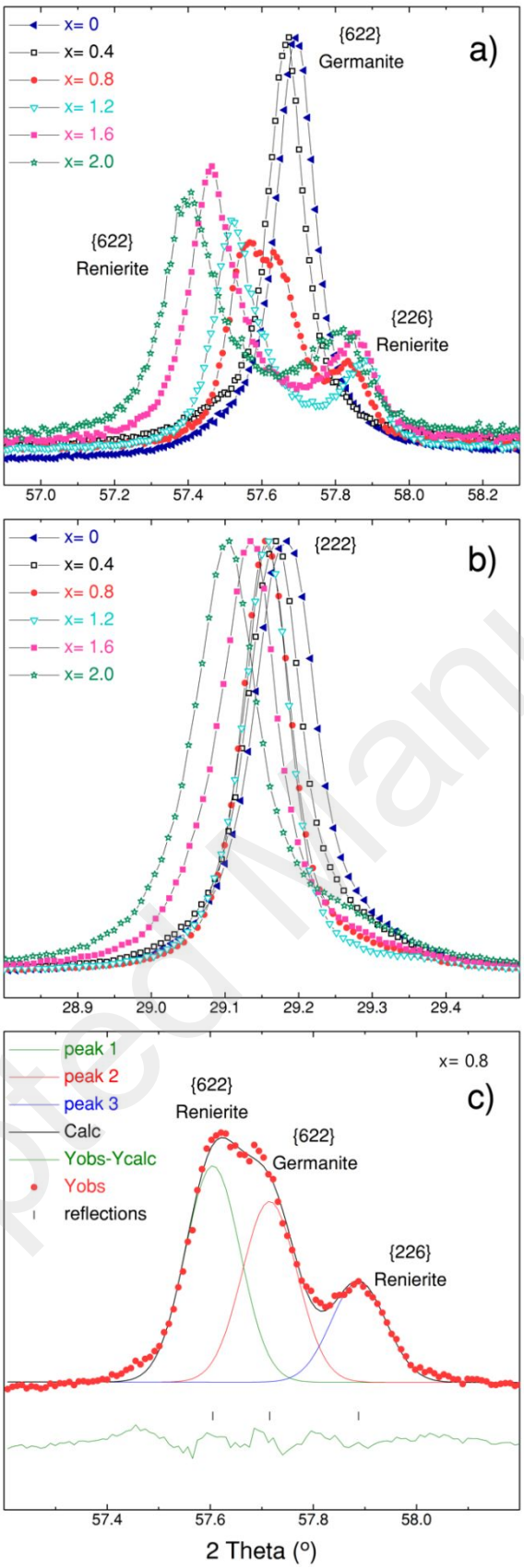

Figure 3. Evolution of a) (622) and b) (222) reflections with Zn content in the $Cu_{22-x}Zn_xFe_8Ge_4S_{32}$ ($0 \leq x \leq 2$) series. c) Profile fitting of the (622) peaks for $x = 0.8$ sample.

To confirm the germanite structure for samples with $x \leq 0.4$, PEDT data were collected on a single crystal (size ~200 nm) for a sample $x = 0$. In **Fig. 4a**, the reciprocal space section 0*kl* reconstructed from PEDT data exhibit extra reflections compatible with the cubic primitive lattice of the germanite. The $P\bar{4}3n$ space group is further confirmed from the *hkh* and *hhl* sections in **Fig. 4c and 4d**, respectively, where the condition limiting the reflections *hkh*: $k = 2n$ and *hhl*: $l = 2n$ is clearly observed.

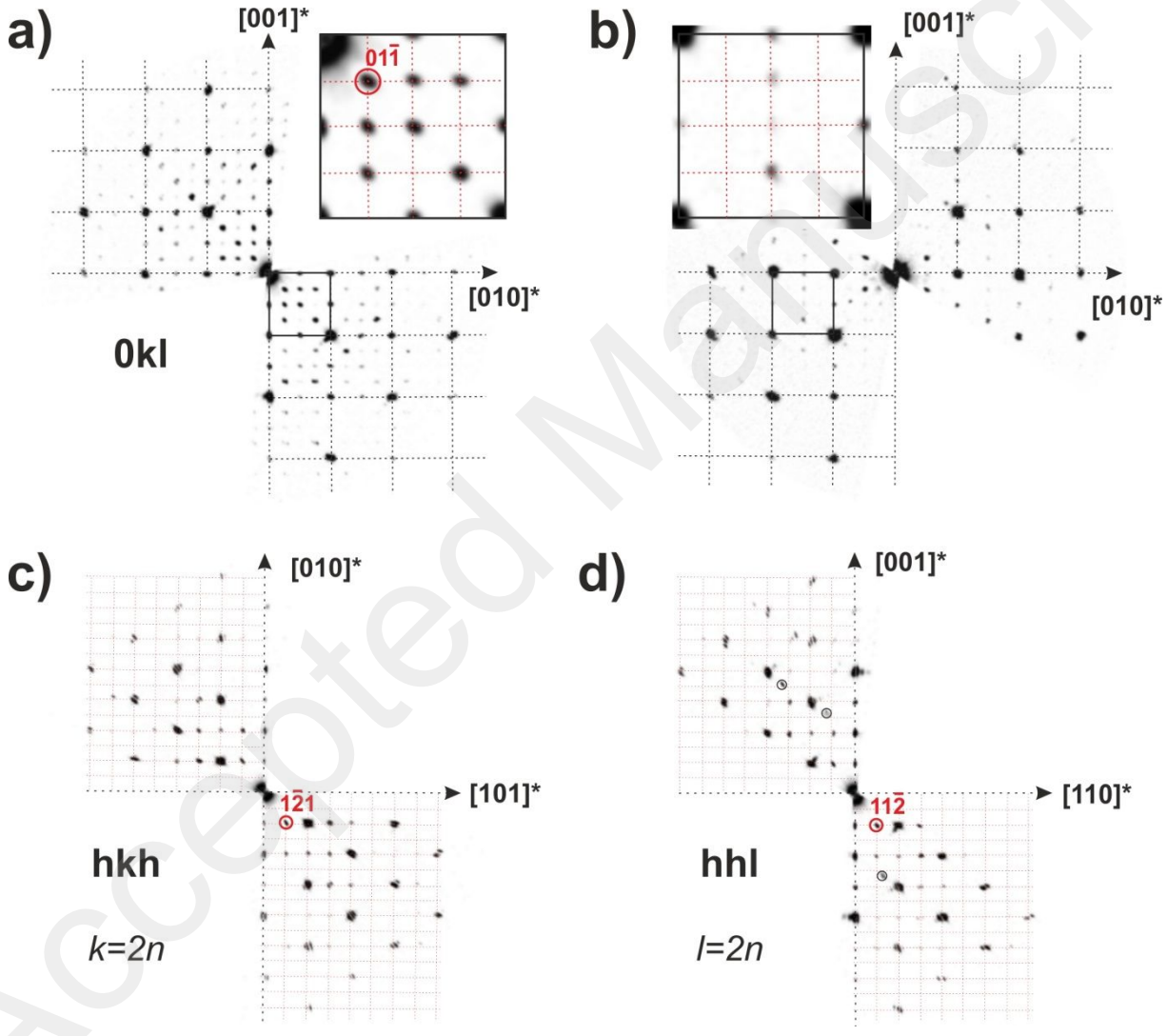

Figure 4. Reciprocal space sections reconstructed from PEDT data for samples $Cu_{22-x}Zn_xFe_8Ge_4S_{32}$ with in: a) 0*kl* section for $x = 0$, b) 0*kl* section for $x = 2$, c) *hkh* section for $x = 0$ and d) *hhl* section for $x = 0$. In a) and b), the reflections related to the sphalerite subcell are highlighted using black dotted lines. In a) and b), the enlarged inserts are used to better view

extra supercell reflections signing the existence of an ordering with respect to the sphalerite subcell. Red dotted lines are used as a guide to the eyes to visualize the reciprocal lattice mesh.

Bearing in mind that the cationic distribution in both structures is complex due to disorder phenomena, Rietveld refinements from PXRD data are not expected to be of much help to elucidate ordering phenomena in such samples due to the equivalent scattering factors of the cations. It is especially the case in renierite where most of the crystallographic sites exhibit a simultaneous occupancy by two different cations involving either statistical or semi-ordered distributions.[24] Considering this difficulty, only Le Bail refinements were used to fit the diffraction data in order to distinguish the two different structures. This is illustrated for the x = 0.8 biphasic sample which peak profiles suggest that the latter corresponds to a mixture of germanite and renierite phases (**Fig. 3c**). This is confirmed by refinements leading to a mixture of germanite with a = 10.598(1) Å and renierite with a = 10.620(1) Å and c = 10.554(2) Å. Due to the overlapping of the diffraction peaks of germanite and renierite, it is difficult to determine accurately the proportion of each phase in this sample. However, a peak profile fitting of the (622) peaks indicates that the area corresponding to the (622) peak of the germanite phase represents ≈ 36% of the total area, while it is of ≈ 42% and ≈ 22% for the (622) and (226) peaks of the renierite phase, respectively (**Fig. 3c**). Considering that the 2 for 1 intensity ratio expected for the (622) and (226) peaks of renierite is well reproduced, we can estimate the proportion of germanite and renierite phases in the x = 0.8 sample to be ≈ 1/3 and ≈ 2/3, respectively.

Note that the intensity of the superstructure diffraction peaks of renierite are strongly reduced for higher Zn content samples. This is confirmed by PEDT collected on a x = 2 sample (**Fig. 4b**) where the 0kl reciprocal space section shows mostly strong reflections related to the sphalerite subcell. In the insert of **Fig. 4b**, weak superstructure reflections confirm the existence

of an ordering with respect to the sphalerite with, at least, one cell parameter of about 10.6 Å. Due to the weakness of the extra reflections and the presence of systematic twinning in the PEDT data, no conclusive result can be obtained regarding the possible space groups for this sample. This nonetheless suggests that an ordering compatible with both the briartite (Cu_2FeGeS_4, $I\bar{4}2m$, a = 5.32 Å, c = 10.55 Å, see in **Fig. 1e**) and the renierite structure should be considered for the refinements of samples for which $x \geq 1.2$. However, in the briartite, both metal/sulfur ratio (equal to 1) and chemical composition differ significantly from our nominal chemical compositions, especially the Cu:Ge ratio. This should induce the existence of at least one secondary phase, which is not observed on the experimental PXRD patterns. Moreover, our nominal chemical compositions are coherent with the chemical compositions of natural renierite $(Cu,Zn)_{22}Fe_8(Ge,As)_4S_{32}$.[24] Last but not least, ^{57}Fe hyperfine parameters of samples, for which $x \geq 1.2$ determined from fits of RT Mössbauer spectra (see below), are much smaller than those expected for a briartite structure. Consequently, the multiple evidences are clearly in favor of a renierite structure. Consequently, it is reasonable to consider that higher Zn content samples exhibit a renierite-type structure in which the cationic site distribution is highly disordered, inducing the reduction of intensity of the superstructure diffraction peaks. This is supported by the complex crystal structure of renierite, where a partial occupancy of the cationic sites was reported by Bernstein *et al.*,[24] and by the synthesis and sintering conditions used to prepare our samples. Indeed, these conditions are well-known to be favorable to structural disorder. Such structural disorder associated with superstructure diffraction peaks extinction was also observed in closely related colusite structures.[21] From these considerations, the refinements of the PXRD patterns of the x = 1.2, x = 1.6, and x = 2.0 samples were finally carried out by considering a renierite crystal structure.

The evolution of the refined unit cell parameters of germanite/renierite-type phases versus Zn content is shown in **Fig. 5.** From this figure, it could be noted that the *a* parameter of the cubic

germanite is intermediate between the *a* and *c* parameters of the tetragonal renierite.-Moreover, a linear variation of the *a* parameter of renierite with Zn content is observed, and the same trend is evidenced for germanite. Hence, by considering those linear tendencies and the refined unit cell parameters *a* for germanite and renierite phases in the $x = 0.8$ sample, it is possible to estimate the "real" Zn content which delimits the germanite and renierite domains to be $0 \leq x \leq 0.6$ and $1.0 \leq x \leq 2.0$, respectively.

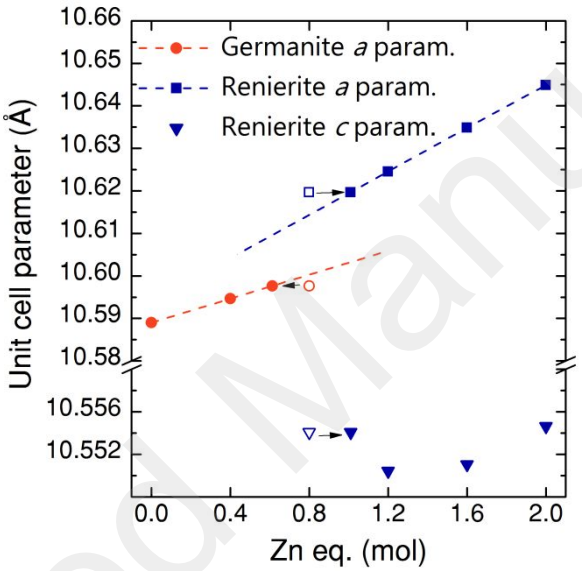

Figure 5. Evolution of the refined unit cell parameters of germanite/renierite phases versus Zn content in the $Cu_{22-x}Zn_xFe_8Ge_4S_{32}$ ($0 \leq x \leq 2$) series.

Qualitative characteristics of room-temperature Mössbauer spectra

Mössbauer spectra of $Cu_{22-x}Zn_xFe_8Ge_4S_{32}$ with x ($0 \leq x \leq 2.0$), recorded at room-temperature (RT) between -2.5 mm/s and 2.5 mm/s, are shown in **Fig. 6** for $x = 0$, 0.4, 0.8, 1.2, and 2.0. Solid lines, except for $x = 0.8$, are obtained from least-squares fits of the spectra that will be discussed later on. An asymmetrical shape of the main central component characterizes the

spectrum with $x = 0$ while the spectra ($x = 1.2$, 2.0) have central parts that are also asymmetrical but broader than the one with $x = 0$. Intermediate spectra ($x = 0.4$, 0.8) are less asymmetrical with somewhat flattened central parts.

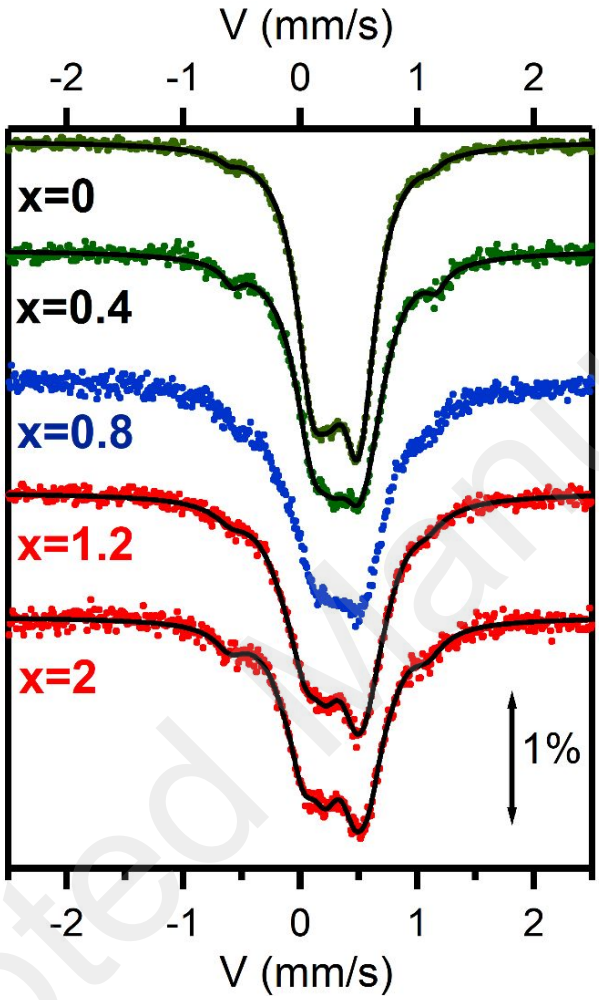

Figure 6. Room-temperature ^{57}Fe Mössbauer spectra of $Cu_{22-x}Zn_xFe_8Ge_4S_{32}$ for $x = 0$, 0.4, 0.8, 1.2, and 2.0. Black solid lines are results of least-squares fits in conditions described in the text.

All the spectra show peaks at *ca*. -0.5 mm/s and *ca*. 1 mm/s, whose central lines are associated with a magnetic phase as clearly shown by the spectrum of $Cu_{20}Zn_2Fe_8Ge_4S_{32}$ ($x = 2.0$) recorded between -8 mm/s and 8 mm/s (**Fig. 7**). Altogether, the magnetic spectrum of **Fig. 7** is complicated with its broad external and intermediate lines. The largest hyperfine magnetic field

at RT is <B> ~36 T for $x = 0$ and <B> ~35.4 T for $x = 2.0$. We recall that the hyperfine magnetic field of α-Fe at RT is 33.1 T. The assumption of similar Lamb-Mössbauer factors for all phases leads to estimate that on the average ~25% of the total Fe might be contained in the magnetic phase, the maximum value of ~37% occurring for the "$Cu_{20}Zn_2Fe_8Ge_4S_{32}$" sample. There is no possibility to obtain the observed <B>'s from a combination of Fe with one or more than one element chosen among Cu, Zn and Ge. Then, the magnetic phase includes Fe atoms, up to ~3 Fe for $x = 2.0$, and probably other metallic elements and sulfur atoms. It is worth mentioning that the studied samples are not attracted to a strong permanent magnet at RT. A Mössbauer spectrum of the $x = 2.0$ sample, recorded at 4.2 K, shows that the main phase becomes also magnetic (data not shown). The maximum hyperfine magnetic field of this mixture of two magnetic phases is ~36.4 T, a maximum close to the maximum field, 35.4 T, found at RT. The Mössbauer spectrum recorded at 4.2 K is however too complex to be fitted reliably.

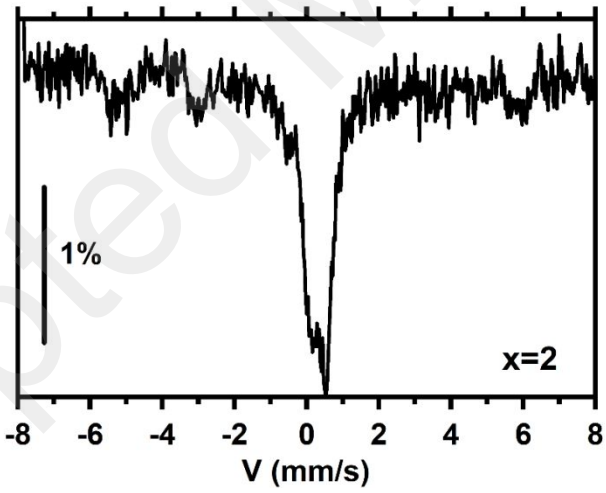

Figure 7. Room-temperature ^{57}Fe Mössbauer spectrum of $Cu_{20}Zn_2Fe_8Ge_4S_{32}$ in a velocity range (-8 mm/s, +8 mm/s).

The velocity intervals between the central lines of the previous magnetic phases are 1.73 (5), 1.70 (4), 1.63 (4), and 1.69 (3) for $x = 0$, 0.4, 1.2, and 2.0 respectively. The average position of

the center of gravity of these lines is 0.26 (3) mm/s. The area fractions of the central peaks of magnetic components, *y*, normalized to the total spectral areas measured between -2.5 mm/s and +2.5 mm/s, increase with *x*. The *y* values are 0.02(1), 0.04(2), 0.06(2), and 0.09(2) for x = 0, 0.4, 1.2, and 2.0 respectively. The area fractions associated with the magnetic phase are estimated by assuming that the intensity ratios of peaks of sextuplets are the theoretical ones for thin absorbers, *i.e.* 3 for external lines, 2 for intermediate lines and 1 for central lines. If the central area fraction of the magnetic phase is *y*, then its total area is $(3+2+1)y = 6y$ when all peaks are included. The total area of the non-magnetic phase is by definition $1-y$. The total area of the two phases is $1+5y$. Finally, the area fractions of the magnetic phase are estimated to be given by $6y/(1+5y)$, that is 0.11, 0.20, 0.28, and 0.37 for x = 0, 0.4, 1.2, and 2.0, respectively, with an average of 0.24. The number of Fe atoms in the magnetic phase increases accordingly between ~1 and ~3 when *x* increases from 0 to 2.0 with the additional assumption of equal Lamb-Mössbauer factors for all Fe sites. For reasons explained below, no value is given for x = 0.8.

These magnetic contributions may result from the presence of magnetic secondary phases, thus implying some significant changes of actual compositions with respect to nominal ones. However, the selectivity of ^{57}Fe Mössbauer spectroscopy makes these magnetic phases clearly visible despite the fact that their atomic fractions in the studied samples are possibly small. An alternative hypothesis to account for the presence at RT of a magnetic contribution in all samples is that the magnetic contribution is intrinsic to the germanite/renierite structure in which iron sublattices with different magnetic ordering temperatures would coexist. This might explain why powder X-ray diffraction fails to detect this “secondary phase”. The close values of maximum hyperfine magnetic fields at 4.2 K and at RT mean that the magnetic phase has its magnetic transition temperature well above RT. However, the validation of those assumption

requires a perfect knowledge of both crystal and magnetic structure of germanite/renierite systems. Such determinations are in progress.

Hereafter, we discuss no more the previous central lines due to the magnetic contribution at RT and we continue to use the nominal compositions. Only the two or three components of the central part of any spectrum that is relevant to the studied phases are numbered, starting with 1 and the sum of their area fractions is normalized to 1.

Fig. 6 shows that the main components of the spectra are packed with peaks (at least four) from the different sites in narrow velocity ranges. The determination of the exact number of Mössbauer sites is thus problematic all the more than lines may become broader as a consequence of aforementioned structural disorder. Nevertheless, asymmetrical spectra allow us to conclude unambiguously that their central components consist of at least two doublets.

Thinning of RT Mössbauer spectra

To highlight the various iron containing phases and the evolution of spectra with x, we "thin" them with a method described in section 7.2 (page 10759) of ref.[37] The latter performs a deconvolution of a Lorentz line, whose FWHM is chosen here as 0.22 mm/s (the natural linewidth of ^{57}Fe is 0.194 mm/s), from the experimental spectrum with the help of a constrained Hesse-Rübartsch method. This model independent method smoothes thinned spectra in a controlled way to bypass the ill-posed nature of the inverse problem which consists in deriving an underlying distribution from an experimental spectrum.[38] The deconvolution procedure is indeed much the same as using the constrained Hesse-Rübatsch method for determining an isomer shift distribution.[37] The latter method involves a smoothing parameter that must be chosen small enough to avoid distorting excessively the thinned spectrum, and large enough to rub out at best oscillations above a flat zero background which are driven by counting statistics.

Peaks in thinned spectra are thus considered as significant only if their amplitudes are clearly larger than low amplitude fluctuations above the zero background (~ 0.1 in **Fig. 8**). The thinning method yields *in fine* "spectra" whose resolutions are improved and, importantly, whose areas are normalized to 1 so that they are directly comparable (**Fig. 8**). The previous method was used by Hightower *et al.*[39] to study Li-SnO anode materials for Li-ion cells (^{119}Sn Mössbauer isotope). A final remark is that thinned spectra may be fitted in turn with Gaussian or Voigt lines to provide starting values for classical least-squares fitting methods of as-recorded spectra.

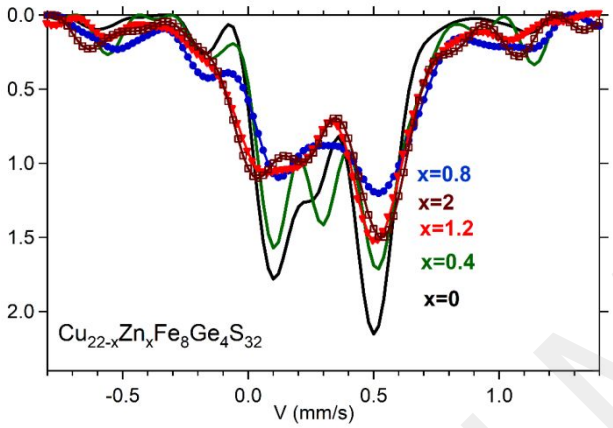

Figure 8. Thinned RT ^{57}Fe Mössbauer spectra of $Cu_{22-x}Zn_xFe_8Ge_4S_{32}$ obtained from as-recorded spectra of **Fig. 6** for x = 0, 0.4, 0.8, 1.2, and 2.0. For the sake of clarity, thinned spectra are plotted in a velocity range narrower than the one of **Fig. 6**. Central peaks of magnetic phase emerge at ~ -0.5 mm/s and ~ 1 mm/s.

Fig. 8 highlights a first pair (x = 0, x = 0.4), whose peaks are narrower than those of other spectra, with two high amplitude central peaks and a smaller amplitude peak located between them. A second pair (x = 1.2, x = 2.0) is made up of almost identical spectra with peaks broader than those of the first pair. Narrow « valleys » are seen at ~ 0.3 mm/s. The x = 0.8 spectrum differs from the previous ones. It bears a reminiscence of the two intense peaks of the first pair, though broader, with a broad and flat region between them. This region might result from a weighted sum of a peak and of a valley.

The previous characteristics are fully consistent with the conclusions, based on X-ray diffraction patterns, according to which germanite and renierite structures are formed for $x \leq 0.4$ and $1.2 \leq x \leq 2.0$, respectively, while the $x = 0.8$ sample belongs to a two-phase domain.

Least-squares fits of RT Mössbauer spectra

As suggested by the thinned spectra of **Fig. 8**, as-recorded spectra may be least-squares fitted with either two doublets, two doublets and a singlet or three doublets accordingly to Zn content. As far as possible, FWHM's are free to vary from doublet to doublet but peaks of a given doublet are constrained to have identical amplitudes and FWHM's. However, the narrowness of the central component leads sometimes to unreliable results with FWHM's less than the natural linewidth as peaks overlap strongly. In that case, all fitted peaks are constrained to have the same FWHM's.

Cases of $x = 0$ and $x = 0.4$ samples

Mössbauer sites, more particularly for $x = 0$ and $x = 0.4$, are crowded into a restricted velocity range. This makes it difficult to determine their number. Accordingly, we fitted these spectra with two doublets, two doublets and a singlet, and three doublets with FWHM's either free to vary or constrained to be all equal. The solid lines of **Fig. 6** for $x = 0$ and $x = 0.4$ samples are obtained when fitting with two doublets and a singlet, all with the same FWHM. The fittings that we performed in the various conditions described above show that IS and QS of the two main doublets are robust parameters whose respective average values are similar for $x = 0$ and $x = 0.4$ samples (**Table 1**).

Table 1. Average isomer shifts (IS) and quadrupole splittings (QS) of the two main doublets for $x = 0$ and $x = 0.4$ samples found from all fits

Doublet N°		IS (mm/s)	QS (mm/s)	Γ (mm/s)
1	$x = 0$	0.28±0.02	0.37±0.03	0.32±0.02
	$x = 0.4$	0.29±0.02	0.37_5±0.03	0.37±0.02
2	$x = 0$	0.40±0.03	0.31±0.02	0.30±0.04
	$x = 0.4$	0.44±0.04	0.31±0.04	0.34±0.04

The results shown in **Table 1** are quite similar to those recently published.[16] There are no differences between fits performed with the previous doublets adding either a singlet or a doublet because the latter has an almost zero QS (~ 0.03(3) mm/s). All FWHM's (*i.e.* Γ) are constrained to be the same in the final fits (**Fig. 6**). Singlets have FWHM's of 0.32(1) mm/s and 0.36(1) mm/s while IS's are equal to 0.30(3) mm/s and 0.27(7) mm/s for $x = 0$ and $x = 0.4$ samples, respectively.

The most sensitive parameters to the fitting assumptions are the area fractions.

a) Fits with two doublets:

If all FWHM's are the same, the area fractions p_1 and p_2 of doublets N°1 and N°2 are $p_1 = 0.54(3)$, $p_2 = 0.46(3)$ for $x = 0$, and $p_1 = 0.52(4)$, $p_2 = 0.48(4)$ for $x = 0.4$. If the latter constraint is removed, the area fractions become $p_1 = 0.81$, $p_2 = 0.19$ for $x = 0$, and $p_1 = 0.73$, $p_2 = 0.27$ for $x = 0.4$. However, in the second case the FWHM's are very different for sites 1 and 2, being 0.34 mm/s and 0.24 mm/s, respectively, for $x = 0$, and 0.38 mm/s and 0.29 mm/s for $x = 0.4$. The value of 0.24 mm/s is approximately equal to the smallest possible FWHM that we measure generally. We are thus led to select the first set of results described above with doublets of identical FWHM's and of nearly equal fractions $p_1 \approx p_2$.

b) fits with two doublets and a singlet:

When a singlet (N° 3) is included in fits, the area fractions become: $p_1 = 0.64(3)$, $p_2 = 0.28(3)$, $p_3 = 0.08(3)$ for $x = 0$, and $p_1 = 0.64(4)$, $p_2 = 0.24(4)$, $p_3 = 0.12(4)$ for $x = 0.4$.

To conclude, the existence of two Fe^{3+} Mössbauer sites in germanite phases (*i.e.* x = 0 and x = 0.4 samples) is unambiguously proven and their hyperfine parameters are obtained. The presence of a third minor Fe^{3+} Mössbauer site in a symmetrical environment (QS ≈ 0) is less firmly established from Mössbauer data only. However, this is in fair agreement with single crystal X-ray results obtained recently on synthetic germanite highlighting that the high symmetry 2*a* site is fully occupied by Fe (unpublished data).

Cases of the x = 1.2 and x = 2.0 samples

The central parts of the spectra of the second family, that are broader than those of the first family (**Fig. 8**), cannot be accounted for with only two doublets. Consequently, final least-squares fits have been carried out with three doublets (**Fig. 6**). The fitting parameters do not differ significantly when FWHM's are constrained to be all equal or are let free to vary separately.

Table 2. Isomer shifts (IS) and quadrupole splittings (QS) of the three doublets used to fit Mössbauer spectra for $x = 1.2$ and $x = 2.0$ samples

Doublet N°		IS (mm/s)	QS (mm/s)	Γ (mm/s)	Area fraction *p*
1	$x = 1.2$	0.25±0.03	0.41±0.06	0.33±0.04	0.45±0.12
	$x = 2.0$	0.24±0.02	0.44±0.04	0.32±0.02	0.49±0.05
2	$x = 1.2$	0.39±0.03	0.33±0.03	0.33±0.03	0.39±0.08
	$x = 2.0$	0.41±0.02	0.37±0.02	0.31±0.02	0.43±0.05
3	$x = 1.2$	0.29±0.10	0.83±0.10	0.39±0.10	0.16±0.12
	$x = 2.0$	0.31±0.07	0.93±0.07	0.31±0.05	0.08±0.05

The hyperfine parameters gathered in **Table 2** are typical of Fe^{3+} ions and are similar for both Zn contents. It should be noted that (i) the hyperfine parameters of sites 1 and 2 are comparable to those of sites 1 and 2 of the first family ($x = 0$ and 0.4, **Table 1**), suggesting some similarities in term of chemical environments, and (ii) the quadrupole splitting of site 3 is the largest one found in the present study, suggesting that the related Fe^{3+} ions are in strongly distorted chemical environment. These pieces of information on the local environment of Fe atoms in this sulfide are in favor of the complex renierite crystal structure instead of the "simple" briartite one, as supposed from PXRD analyses for the $x = 1.2$ and $x = 2.0$ samples. This is confirmed by the huge difference of hyperfine parameters determined from ^{57}Fe Mössbauer spectroscopy between synthetic briartite Cu_2FeGeS_4 [40] and our samples. First, iron atoms are in a +II oxidation state in briartite[40] and in +III oxidation state in our samples (as expected in renierite). Secondly, the quadrupole splitting associated to the doublet in briartite is ~2.56(2) mm/s at RT,[40] while those associated to the different iron sites in our samples are much smaller (*i.e.* ~0.4 mm/s and ~0.9 mm/s, **Table 2**). Hence, ^{57}Fe Mössbauer spectroscopy results indicate unambiguously that the crystal structure of our Zn-rich samples ($x \geq 1.2$) is different from that of briartite. Consequently, these results in association with those obtained from powder X-ray diffraction are in favor of a disordered renierite crystal structure for $x = 1.2$ and $x = 2.0$ samples.

Case of the x = 0.8 sample

As discussed previously, the Mössbauer spectrum recorded for the $x = 0.8$ sample is intermediate between those of the two families discussed above. From PXRD patterns, the studied sample consists of a two-phase mixture. Thus, its spectrum (**Fig. 6** and **Fig. 8**) is expected to consist of at least five doublets that overlap strongly. The a priori values of the hyperfine parameters of all these contributions, which change slightly with x, are not known

with enough precision to attempt to fit reliably the observed spectrum so as to get trustworthy hyperfine parameters. This is the reason why this spectrum is not discussed further.

In summary:

- All the samples contain a phase magnetically ordered at room temperature.
- ^{57}Fe Mössbauer spectra reflect the structural changes evidenced by PXRD patterns that occur in $Cu_{22-x}Zn_xFe_8Ge_4S_{32}$ series when x increases between 0 and 2.0 with a first pair of spectra (x = 0 and 0.4), an intermediate spectrum (x = 0.8), and a second pair of spectra (x = 1.2 and 2.0).
- The central parts of the spectra (other than those of the magnetic contribution) consist unambiguously of at least two sites. In agreement with structural arguments from single crystal X-ray diffraction, the spectra include a third site. The hyperfine parameters are obtained for samples of the two pairs. The narrow velocity ranges which contain the central parts prevent to fit reliably the spectrum with x = 0.8 as this sample is a mixture of two different phases.
- All the measured hyperfine parameters are consistent with iron being in the form of Fe^{3+}.
- Hyperfine parameters determined for Zn-rich samples ($x \geq 1.2$) indicate unambiguously that the crystal structure of the Zn-rich compounds is different from that of briartite.

Thermoelectric properties

The temperature dependences of the electrical resistivity, ρ, and Seebeck coefficient, S, in the $Cu_{22-x}Zn_xFe_8Ge_4S_{32}$ series are displayed in **Fig. 9a and 9b** respectively. Regardless of the Zn

content, a positive value for the Seebeck coefficient is measured, confirming holes as dominant charge carriers. For $x = 0$, the electrical resistivity, which decreases slightly as the temperature increases, shows that this material exhibits a semiconducting behavior, though approaching the transition towards a metallic state. The Seebeck coefficient varies slightly with temperature and in opposite trend relative to the electrical resistivity. This behavior is explained by the fact that the conduction regime is intermediate between metallic and semiconducting. When the Zn content increases, the magnitude of the electrical resistivity increases drastically at 300 K from 9.3 mΩ cm for $x = 0$ to 2.57×10^3 mΩ cm for $x = 2.0$. The Seebeck coefficient also increases with the Zn content from +122 μV K^{-1} for $x = 0$ to +262 μV K^{-1} for $x = 2.0$ at 300 K. The temperature dependences of ρ and S for $x = 2.0$ tend toward a semiconducting behavior, as observed from the sharper decrease of ρ (plotted in log scale) with the increase of temperature. This behavior is consistent with a decrease of the carrier concentration. Indeed, from a formal charge point of view, stoichiometric $Cu_{22}Fe_8Ge_4S_{32}$ is assumed to be $(Cu^+)_{20}(Cu^{2+})_2(Fe^{3+})_8(Ge^{4+})_4(S^{2-})_{32}$. By analogy to $Cu_{12}Sb_4S_{13}$ tetrahedrite, there are two unoccupied states in the valence band above E_F. Therefore, the unoccupied states in such a compound could be filled by substituting Cu by a divalent transition element (Zn), as also reported in tetrahedrite and colusite,[6,18] leading to a semiconducting behavior. In other words, since Zn, Fe and Ge ions are strictly in the Zn^{2+}, Fe^{3+} and Ge^{4+} states, the increase of S and ρ with x is consistent with a decrease in Cu^{2+} content, *i.e.*, of hole concentration. On the other hand, the introduction of additional Zn^{2+} cations on the copper sites likely decreases the mobility of carriers due to the creation of point defects, which perturbates the percolation paths in the tridimensional "Cu-S" conductive network. Unfortunately, the variation of the carrier concentration with x was not verified as it was impossible to extract reliable carrier concentration values from Hall effect measurements due to an anomalous signal. Finally, the

significant increase of the electrical resistivity with x induces a decrease of the power factor from 0.29 mW m^{-1} K^{-2} for $x = 0$ to 0.11 mW m^{-1} K^{-2} for $x = 2.0$, at 700 K (**Fig. 9e**).

The temperature dependence of the thermal conductivity in the $Cu_{22-x}Zn_xFe_8Ge_4S_{32}$ series (**Fig. 9c**) exhibits a systematic decrease of the thermal conductivity with increasing Zn content. This reflects the combined effects of a reduced electronic component of the thermal conductivity and a decreasing lattice contribution. By simply subtracting the electronic part from the total thermal conductivity, it can be observed that a higher Zn content (especially above $x = 0.8$) causes marked reductions in the lattice thermal conductivities of these compounds over the full temperature range (**Fig. 9d**). In fact, two distinct sets of values can be observed depending of the Zn content. For $0 \leq x \leq 0.4$, the lattice thermal conductivity values are in the ranges of 1.60-1.65 W m^{-1} K^{-1} at 300 K and 0.90-0.95 W m^{-1} K^{-1} at 700 K, while for $1.2 \leq x \leq 2.0$, the lattice thermal conductivity drops down to 1.13-1.25 W m^{-1} K^{-1} at 300 K and 0.70 W m^{-1} K^{-1} at 700 K. Interestingly, the $x = 0.8$ sample, composed of both renierite and germanite, exhibits intermediate values around 1.45 W m^{-1} K^{-1} at 300 K and 0.80 W m^{-1} K^{-1} at 700 K. This trend suggests that the additional number of crystallographic sites and the higher cationic disorder in the renierite-type compounds ($1.2 \leq x \leq 2.0$), induced by the tetragonal distortion, provides an effective way of scattering heat carrying phonons. Unfortunately, the crystal structure of our synthetic renierite-type compounds being quite complex (as discussed in the structure analysis section), it was not possible to perform phonon calculations and to address the role of specific crystal structure features on phonon scattering. Finally, it must be pointed out that the κ_L values of the Zn-rich compounds ($1.2 \leq x \leq 2.0$) are in the same range as those of other copper-based sulfide minerals such as pristine $Cu_8Fe_3Sn_2S_{12}$ stannoidite,[15] and ordered colusites.[20,22]

From the above parameters, the figure of merit, ZT, was calculated for all the samples and displayed in **Fig. 9f**. Overall, the ZT increases with temperature for all compositions. Due to the

counter-balanced effects of the decrease of both the power factor and the thermal conductivity, the *ZT* remains constant for Zn content below $x \leq 1.6$ and decreases significantly for $x = 2.0$ due to the large increase of the electrical resistivity.

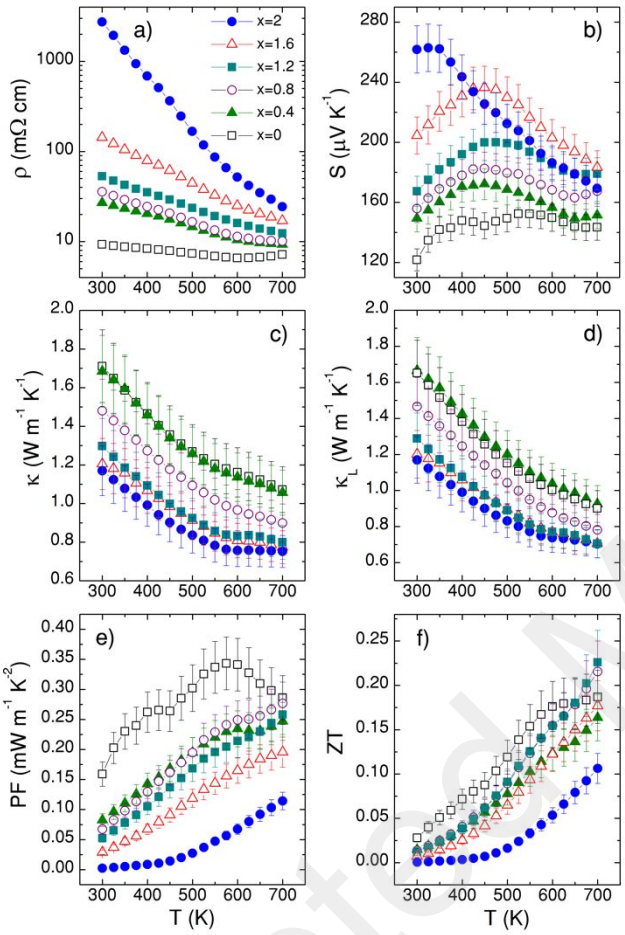

Figure 9. Temperature dependences of a) electrical resistivity (ρ), b) Seebeck coefficient (S), c) thermal conductivity (κ), d) lattice thermal conductivity (κ_L), e) power factor (PF), and f) figure of merit (ZT) in the in the $Cu_{22-x}Zn_xFe_8Ge_4S_{32}$ ($0 \leq x \leq 2.0$) series.

Conclusion

A thermoelectric sulfide $Cu_{22-x}Zn_xFe_8Ge_4S_{32}$ ($1.2 \leq x \leq 2.0$) with the renierite-type structure has been synthesized for the first time. The close structural relationship between this sulfide and the germanite shows that its conductive "Cu-S" network, as in germanite, constitutes a driving force for the appearance of *p*-type hole carriers and consequently of thermoelectric properties in this material. It appears clearly that the zinc concentration has a correlated effect on both the electrical and thermal conductivity in these sulfides. Increasing the Zn concentration in the copper network leads to a decrease in the concentration of hole carriers, *i.e.* to an increase of the electrical resistivity and Seebeck coefficient in renierite compared to germanite. However, the cationic disorder in the copper network increases with the Zn content and results in a decrease in the thermal conductivity that ultimately becomes lower for renierite with respect to germanite. This explains the very similar figures of merit that are observed for both structural types independently of the zinc content. Further investigations on univalent copper-rich systems should be encouraged for enhancing the performances of *p*-type thermoelectric materials.

Acknowledgements

The authors would like to thank Christelle Bilot and Jerôme Lecourt for technical support and the financial support of the French Agence Nationale de la Recherche (ANR), through the program Energy Challenge for Secure, Clean and Efficient Energy (Challenge 2, 2015, ANR-15-CE05-0027).

Author Information

Corresponding Authors

E-mail: emmanuel.guilmeau@ensicaen.fr, phone: +33 231 451 367.

Email : pierric.lemoine@univ-rennes1.fr, phone : +33 223 233 306.

Author Contributions

The manuscript was written through contributions of all authors. All authors have given approval to the final version of the manuscript.

Funding Sources

French Agence Nationale de la Recherche (ANR), through the program Energy Challenge for Secure, Clean and Efficient Energy (Challenge 2, 2015, ANR-15-CE05-0027).

References

(1) Qiu, P.; Zhang, T.; Qiu, Y.; Shi, X.; Chen, L. Sulfide Bornite Thermoelectric Material: A Natural Mineral with Ultralow Thermal Conductivity. *Energy Environ. Sci.* **2014**, *7*, 4000.

(2) Guélou, G.; Powell, A. V.; Vaqueiro, P. Ball Milling as an Effective Route for the Preparation of Doped Bornite: Synthesis, Stability and Thermoelectric Properties. *J. Mater. Chem. C* **2015**, *3*, 10624–10629.

(3) Pavan Kumar, V.; Barbier, T.; Lemoine, P.; Raveau, B.; Nassif, V.; Guilmeau, E. The Crucial Role of Selenium for Sulphur Substitution in the Structural Transitions and Thermoelectric Properties of Cu_5FeS_4 Bornite. *Dalt. Trans.* **2017**, *46*, 2174.

(4) Long, S. O. J.; Powell, A. V; Vaqueiro, P.; Hull, S. High Thermoelectric Performance of Bornite through Control of the Cu(II) Content and Vacancy Concentration. *Chem. Mater.* **2018**, *30*, 456–464.

(5) Suekuni, K.; Tsuruta, K.; Ariga, T.; Koyano, M. Thermoelectric Properties of Mineral Tetrahedrites $Cu_{10}Tr_2Sb_4S_{13}$ with Low Thermal Conductivity. *Appl. Phys. Express* **2012**, *5*, 051201.

(6) Suekuni, K.; Tsuruta, K.; Kunii, M.; Nishiate, H.; Nishibori, E.; Maki, S.; Ohta, M.; Yamamoto, A.; Koyano, M. High-Performance Thermoelectric Mineral $Cu_{12-x}Ni_xSb_4S_{13}$ Tetrahedrite. *J. Appl. Phys.* **2013**, *113*, 043712.

(7) Lu, X.; Morelli, D. T.; Xia, Y.; Zhou, F.; Ozolins, V.; Chi, H.; Zhou, X.; Uher, C. High Performance Thermoelectricity in Earth-Abundant Compounds Based on Natural Mineral Tetrahedrites. *Adv. Energy Mater.* **2013**, *3*, 342–348.

(8) Barbier, T.; Lemoine, P.; Gascoin, S.; Lebedev, O. I.; Kaltzoglou, A.; Vaqueiro, P.; Powell, A. V.; Smith, R. I.; Guilmeau, E. Structural Stability of the Synthetic Thermoelectric Ternary and Nickel-Substituted Tetrahedrite Phases. *J. Alloys Compd.* **2015**, *634*, 253–262.

(9) Chetty, R.; Bali, A.; Mallik, R. C. Tetrahedrites as Thermoelectric Materials : An Overview. *J. Mater. Chem. C* **2015**, *3*, 12364–12378.

(10) Bouyrie, Y.; Candolfi, C.; Ohorodniichuk, V.; Malaman, B.; Dauscher, A.; Tobola, J.; Lenoir, B. Crystal Structure, Electronic Band Structure and High-Temperature Thermoelectric Properties of Te-Substituted Tetrahedrites $Cu_{12}Sb_{4-x}Te_xS_{13}$ ($0.5 \leq x \leq 2.0$). *J. Mater. Chem. C* **2015**, *3*, 10476–10487.

(11) Barbier, T.; Rollin-Martinet, S.; Lemoine, P.; Gascoin, F.; Kaltzoglou, A.; Vaqueiro, P.; Powell, A. V.; Guilmeau, E. Thermoelectric Materials: A New Rapid Synthesis Process for Nontoxic and High-Performance Tetrahedrite Compounds. *J. Am. Ceram. Soc.* **2016**, *99*, 51–56.

(12) Barbier, T.; Lemoine, P.; Martinet, S.; Eriksson, M.; Gilmas, M.; Hug, E.; Guélou, G.; Vaqueiro, P.; Powell, A. V; Guilmeau, E. Up-Scaled Synthesis Process of Sulphur-Based Thermoelectric Materials. *RSC Adv.* **2016**, *6*, 10044–10053.

(13) Liu, M. L.; Huang, F. Q.; Chen, L. D.; Chen, I. W. A Wide-Band-Gap p-Type Thermoelectric Material Based on Quaternary Chalcogenides of Cu_2ZnSnQ_4 (Q = S,Se). *Appl. Phys. Lett.* **2009**, *94*, 202103.

(14) Yang, H.; Jauregui, L. A.; Zhang, G.; Chen, Y. P.; Wu, Y. Non-Toxic and Abundant Copper Zinc Tin Sulfide Nanocrystals for Potential High Temperature Thermoelectric Energy Harvesting. *Nano Lett.* **2012**, *12*, 540–545.

(15) Pavan Kumar, V.; Barbier, T.; Caignaert, V.; Raveau, B.; Daou, R.; Malaman, B.; Le Caër, G.; Lemoine, P.; Guilmeau, E. Copper Hyper-Stoichiometry: The Key for the Optimization of Thermoelectric Properties in Stannoidite $Cu_{8+x}Fe_{3-x}Sn_2S_{12}$. *J. Phys. Chem. C* **2017**, *121* (30), 16454–16461.

(16) Pavan Kumar, V.; Paradis-Fortin, L.; Lemoine, P.; Caignaert, V.; Raveau, B.; Malaman, B.; Le Caër, G.; Cordier, S.; Guilmeau, E. Designing a Thermoelectric Copper-Rich Sulfide from a Natural Mineral: Synthetic Germanite $Cu_{22}Fe_8Ge_4S_{32}$. *Inorg. Chem.* **2017**, *56* (21), 13376–13381.

(17) Suekuni, K.; Kim, F. S.; Nishiate, H.; Ohta, M.; Tanaka, H. I.; Takabatake, T. High-Performance Thermoelectric Minerals : Colusites $Cu_{26}V_2M_6S_{32}$ (M = Ge, Sn). *Appl. Phys. Lett.* **2014**, *105*, 132107.

(18) Suekuni, K.; Kim, F. S.; Takabatake, T. Tunable Electronic Properties and Low Thermal Conductivity in Synthetic Colusites $Cu_{26-x}Zn_xV_2M_6S_{32}$ ($x \leq 4$, M = Ge, Sn). *J. Appl. Phys.* **2014**, *116*, 063706.

(19) Kikuchi, Y.; Bouyrie, Y.; Ohta, M.; Suekuni, K.; Aihara, M.; Takabatake, T. Vanadium-Free Colusites $Cu_{26}A_2Sn_6S_{32}$ (A = Nb, Ta) for Environmentally Friendly Thermoelectrics. *J. Mater. Chem. A* **2016**, *4* (39), 15207–15214.

(20) Bourgès, C.; Bouyrie, Y.; Supka, A. R.; Al Rahal Al Orabi, R.; Lemoine, P.; Lebedev, O. I.; Ohta, M.; Suekuni, K.; Nassif, V.; Hardy, V.; Daou, R.; Miyazaki, Y.; Fornari, M.; Guilmeau, E. High-Performance Thermoelectric Bulk Colusite by Process Controlled Structural Disordering. *J. Am. Chem. Soc.* **2018**, *140* (6), 2186–2195.

(21) Suekuni, K.; Shimizu, Y.; Nishibori, E.; Kasai, H.; Saito, H.; Yoshimoto, D.; Hashikuni, K.; Bouyrie, Y.; Chetty, R.; Ohta, M.; Guilmeau, E.; Takabatake, T.; Watanabe, K.;

Ohtaki, M. Atomic-Scale Phonon Scatterers in Thermoelectric Colusites with a Tetrahedral Framework Structure. *J. Mater. Chem. A* **2019**, *7* (1), 228–235.

(22) Pavan Kumar, V.; Supka, A. R.; Lemoine, P.; Lebedev, O. I.; Raveau, B.; Suekuni, K.; Nassif, V.; Al Rahal Al Orabi, R.; Fornari, M.; Guilmeau, E. High Power Factors of Thermoelectric Colusites $Cu_{26}T_2Ge_6S_{32}$ (T = Cr, Mo, W): Toward Functionalization of the Conductive "Cu–S" Network. *Adv. Energy Mater.* **2019**, *9*, 1803249.

(23) Pavan Kumar, V.; Guélou, G.; Lemoine, P.; Raveau, B.; Supka, A. R.; Fornari, M.; Suekuni, K.; Guilmeau, E. Copper-Rich Thermoelectric Sulfides: Size Mismatch Effect and Chemical Disorder in the $[TS_4]Cu_6$ Complexes of $Cu_{26}T_2Ge_6S_{32}$ (T = Cr,Mo,W) Colusites. *Angew. Chemie, Int. Ed.* **2019**. (In press, DOI: 10.1002/anie.201908579)

(24) Bernstein, L. R.; Reichel, D. G.; Merlino, S. Renierite Crystal Structure Refined from Rietveld Analysis of Powder Neutron-Diffraction Data. *Am. Mineral.* **1989**, *74* (9–10), 1177–1181.

(25) Rodríguez-Carvajal, J. Recent Advances in Magnetic Structure Determination by Neutron Powder Diffraction. *Phys. B Condens. Matter* **1993**, *192* (1–2), 55–69.

(26) Roisnel, T.; Rodríguez-Carvajal, J. WinPLOTR: A Windows Tool for Powder Diffraction Patterns Analysis. *Mater. Sci. Forum* **2001**, *378–381*, 118–123.

(27) Mugnaioli, E.; Gorelik, T.; Kolb, U. "ab Initio" Structure Solution from Electron Diffraction Data Obtained by a Combination of Automated Diffraction Tomography and Precession Technique. *Ultramicroscopy* **2009**, *109* (6), 758–765.

(28) Boullay, P.; Palatinus, L.; Barrier, N. Precession Electron Diffraction Tomography for Solving Complex Modulated Structures: The Case of $Bi_5Nb_3O_{15}$. *Inorg. Chem.* **2013**, *52* (10), 6127–6135.

(29) Palatinus, L.; Brázda, P.; Jelínek, M.; Hrdá, J.; Steciuk, G.; Klementová, M. Specifics of the data processing of precession electron diffraction tomography data and their implementation in the program *PETS2.0, Acta Crystallogr. B* **2019**, *75,* 512.

(30) Petříček, V.; Dušek, M.; Palatinus, L. Crystallographic Computing System Jana2006: General Features. *Zeitschrift fur Krist.* **2014**, *229*, 345.

(31) Debyatkova, E. D.; Smirnov, I. A. ,. *Fiz. Tverd. Tela, 2-1984* **1960**.

(32) Anselm, A. *Introduction to the Theory of Semiconductors (English Translation)*, English tr.; Mir Publishers, 1981.

(33) Ravich, Y. I.; Efimova, B. A.; Smirnov, I. A. *Semiconducting Lead Chalcogenides (English Translation)*; Stil'bans, L. S., Ed.; SPRINGER SCIENCE, 1970.

(34) Alleno, E.; Bérardan, D.; Byl, C.; Candolfi, C.; Daou, R.; Decourt, R.; Guilmeau, E.; Hébert, S.; Hejtmanek, J.; Lenoir, B.; Masschelein, P.; Ohorodnichuk, V.; Pollet, M.; Populoh, S.; Ravot, D.; Rouleau, O.; Soulier, M. A Round Robin Test of the Uncertainty on the Measurement of the Thermoelectric Dimensionless Figure of Merit of $Co_{0.97}Ni_{0.03}Sb_3$. *Rev. Sci. Instrum.* **2015**, *86*, 011301.

(35) Tettenhorst, R. T.; Corbato, C. E. Crystal Structure of Germanite, $Cu_{26}Ge_4Fe_4S_{32}$, Determined by Powder X-Ray Diffraction. *Am. Mineral.* **1984**, *69*, 943–947.

(36) Frank-Kamenetskaya, O. V; Rozhdestvenskaya, I. V; Yanulova, L. A. New Data on the Crystal Structures of Colusites and Arsenosulvanites. *J. Struct. Chem.* **2002**, *43* (1), 89–100.

(37) Le Caër, G.; Brand, R. A. General Models for the Distributions of Electric Field Gradients in Disordered Solids. *J. Phys. Condens. Matter* **1998**, *10* (47), 10715–10774.

(38) Le Caër, G.; Dubois, J. M. Evaluation of Hyperfine Parameter Distributions from Overlapped Mossbauer Spectra of Amorphous Alloys. *J. Phys. E.* **1979**, *12* (11), 1083–1090.

(39) Hightower, A.; Delcroix, P.; Le Caër, G.; Huang, C.-K.; Ratnakumar, B. V.; Ahn, C. C.; Fultz, B. A [Sup 119]Sn Mössbauer Spectrometry Study of Li-SnO Anode Materials for Li-Ion Cells. *J. Electrochem. Soc.* **2002**, *147* (1), 1–8.

(40) Imbert, P.; Varret, F.; Wintenberger, M. Etude Par Effet Mössbauer de La Briartite (Cu_2FeGeS_4). *J. Phys. Chem. Solids* **1973**, *34* (10), 1675–1682.

Table of Content